

## Viewpoint



# Early Report of the Source Characteristics, Ground Motions, and Casualty Estimates of the 2023 $M_w$ 7.8 and 7.5 Turkey Earthquakes

Wenkai Chen<sup>1</sup>, Gang Rao<sup>2</sup>, Dengjie Kang<sup>1</sup>, Zhifan Wan<sup>3</sup>, Dun Wang<sup>1\*3</sup>

1. Lanzhou Institute of Seismology, China Earthquake Administration, Lanzhou 730000, China

2. School of Geoscience and Technology, Southwest Petroleum University, Chengdu 610500, China

3. State Key Laboratory of Geological Processes and Mineral Resources, School of Earth Sciences, China University of Geosciences, Wuhan 430074, China

 Wenkai Chen: <https://orcid.org/0000-0003-3235-5861>;  Dun Wang: <https://orcid.org/0000-0001-6435-9168>

## INTRODUCTION

At 01:17 UTC (04:17 on local time) on Feb. 6, 2023, a devastating earthquake with a moment magnitude ( $M_w$ ) 7.8 occurred in the Gaziantep, southern Turkey. The earthquake was located at 37.174°N and 37.032°E, with a hypocentral depth of 17.9 km as reported by the United States Geological Survey (USGS). Nine hours later, a  $M_w$  7.5 earthquake occurred in Kahramanmaraş, about 95 km north to the epicenter of the  $M_w$  7.8 earthquake (37.203°E, 38.024°N, depth 10.0 km). The  $M_w$  7.8 earthquake was the most devastating earthquake in Turkey after the 1939  $M$  7.9 Erzincan Earthquake (killed more than 33 000 people). Until 01:16 UTC of Feb. 13 (one week following the  $M_w$  7.8 earthquake), there have been 1 114 earthquakes, including one  $M > 7$ , two  $M$  6–7, 26  $M$  5–6, and 212  $M$  4–5 events according to the European-Mediterranean Seismological Centre (EMSC). Here the magnitude scale is either  $M_w$  or mb.

The Turkey earthquake sequence occurred at the junction of the East Anatolian fault zone (EAFZ) with the Dead Sea fault zone (DSFZ). The seismically active left-lateral EAFZ together with the right-lateral North Anatolian fault zone (NAFZ) accommodate the westward extrusion of the Anatolian microplate with respect to the Eurasian and Arabian plates (Fig. 1a; Jackson and McKenzie, 1984; McKenzie, 1976, 1972). The EAFZ is characterized by pronounced segmentation of faulting (Fig. 1b; Gülerce et al., 2017; Duman and Emre, 2013). To the south, the EAFZ connects with the DSFZ and the Cyprian arc via Amik triple junction (Fig. 1b; Duman and Emre, 2013). The EAFZ and the DSFZ overlap for about 160 km in the Karasu trough bounded by the left-lateral Amanos and Yesemek fault segments, respectively (Fig. 1b). Present GPS observations reveal a slip rate of ~6.8 mm/yr along the Karasu trough (Reilinger et al., 2006). The Yesemek fault segment delimits the eastern margin of the Karasu trough,

which may have generated the 1822  $M_s$  7.5 earthquake (Ambroseys and Jackson, 1998). Further north, the Narli fault segment is the northernmost tip of the DSFZ, consisting of sub-parallel normal faults separated by relay ramps (Duman and Emre, 2013). The 2023  $M_w$  7.8 earthquake occurred at the location between these two faults. Later, another earthquake of  $M_w$  7.5 happened along the roughly east-west trending Cardak fault segment of the EAFZ (see Fig. 1b for the location). The Cardak fault cuts former thrust faults and folds, and has produced prominent left-lateral slip morphology, with a slip rate of ~2.5 mm/yr (Duman and Emre, 2013).

## SOURCE PROCESS

We use data recorded in Alaskan and Canadian seismic stations to back-project the source propagation of the  $M_w$  7.8 and 7.5 earthquakes. The Alaskan and Canadian seismic stations consist of ~295 broadband seismic stations with sampling rate of 100 Hz (Busby and Aderhold, 2020), among which we chose seismic stations with epicenter distances to the Turkey  $M_w$  7.8 earthquake ranging from 70° to 85° with azimuths of 344° to 349°.

The back-projection method can resolve the rupture fault(s) with less requirement of model parameter setting (Ishii et al., 2005; Krüger and Ohrnberger, 2005). Thus, it has been widely applied in studies of source characteristics of earthquakes (Okuwaki et al., 2019; Meng et al., 2016; Wang and Mori, 2016; Fan and Shearer, 2015; Satriano et al., 2012; Yao et al., 2011; Zhang and Ge, 2010; Vallée et al., 2008). In this study, we performed a back-projection method (beamforming over a sliding/moving window), to trace the rupture processes of the two Turkey earthquakes (Wang et al., 2017). The frequency band, length of the stacking window, and the interval between stacking windows, were 0.8–10.0 Hz, 10 s, and 1 s, respectively. The horizontal grid points were setting at depth of 20 km with an interval of 2 km in horizontal plane.

Figure 2 shows the time propagation of the back-projection results. We used the high frequency waveforms in the back-projection, Hence the results mainly represent rupture front propagations.

For the  $M_w$  7.8 earthquake, the rupture propagated bilateral-

\*Corresponding author: wangdun@cug.edu.cn

© China University of Geosciences (Wuhan) and Springer-Verlag GmbH Germany, Part of Springer Nature 2023

Manuscript received February 19, 2023.

Manuscript accepted February 25, 2023.

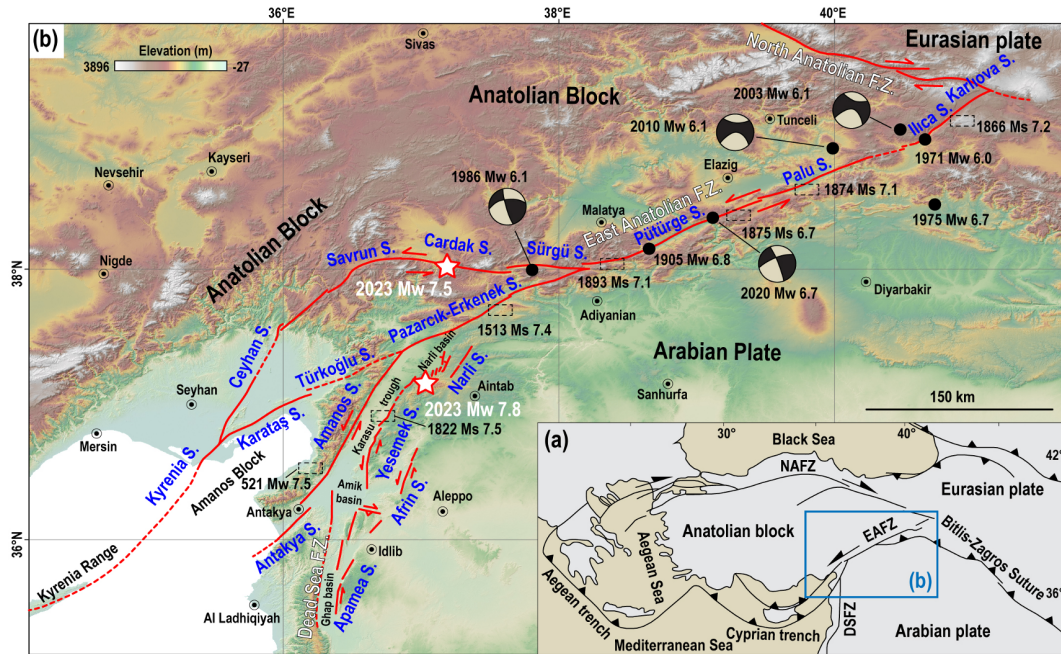


**Figure 1.** Geological environment of the 2023  $M_w$  7.8 and 7.5 damaging earthquakes that occurred at the junction of the East Anatolian fault zone (EAFZ) with the Dead Sea fault zone (DSFZ). (a) Tectonic background of the study area (modified after Gülerce et al., 2017; Duman and Emre, 2013; Kaymakci et al., 2007). (b) The distribution of active fault traces and earthquake epicenters reveals pronounced segmentation of faulting (Gülerce et al., 2017). The 2023  $M_w$  7.8 and 7.5 earthquakes are from the USGS, and the information for the other earthquakes is integrated from Ambraseys and Jackson (1998), Milkereit et al. (2004), Xu et al. (2020), and Lin et al. (2021).

ly along the NE and SW directions. The rupture firstly propagated  $\sim 140$  km along the NE direction for the first 50 s. Then the rupture started to propagate in the SSW direction from the epicenter over a representative length of  $\sim 130$  km for about 30 s. The SSW rupture seems to be more complex; not along a single, straight fault plane, probably in association with multiple, discrete fault segments. The total rupture length and the source duration of the rupture are  $\sim 270$  km and  $\sim 80$  s, respectively. Early aftershocks usually delineate rupture fault(s) of mainshocks (EMSC). Locations of the aftershocks that occurred in the first day following the  $M_w$  7.8 earthquake showed highly compatible fault patterns with the back-projection results.

The  $M_w$  7.5 earthquake also ruptured bilaterally along the W and E directions on the Cardak fault. The rupture expanded  $\sim 60$  km in  $\sim 20$  s in the west direction, and expanded  $\sim 50$  km for  $\sim 30$  s in the east direction according to the distribution of the early aftershocks and the back-projection. The total rupture length and the source duration are 110 km and  $\sim 30$  s, respectively. From the back-projection results, one can observe that the east portion of the ruptured fault was adequately illuminated, while the west portion of the rupture fault was ambiguously recognized.

## GROUND MOTIONS AND EARTHQUAKE CASUALTY ESTIMATION

Based on the back-projection results and a Ground Motion Prediction Equation (GMPE, Si and Midorigawa, 1999), we estimated the Peak Ground Velocity (PGV) fields of the  $M_w$  7.8 and 7.5 the earthquakes (Kang et al., 2023; Chen et al., 2022a, b). Here the attenuation of the seismic intensity was empirically approximated by the GMPE (Si and Midorigawa, 1999), which

employed the closest distance from the back-projected seismic sources. The estimated PGV were then corrected for the site effect using the  $V_{s30}$  data (USGS).

We set a grid of point ( $1 \text{ km} \times 1 \text{ km}$ ) around the source area of  $1000 \text{ km} \times 1000 \text{ km}$ . For each grid, we first calculated the closest distance between the grid point and back-projected source locations. Then we estimated the PGV on stiff ground in each site following Si and Midorigawa (1999). After that, we calculated the site amplification factor for the PGV using the  $V_{s30}$  dataset following Midorigawa (1994). We further converted the PGV on stiff ground to the PGV on the ground surface (PGV $_{Vs30}$ ). The PGV on each grid point was converted to the seismic intensity scale of Modified Mercalli Intensity (MMI, Worden et al., 2012). Hence, the seismic intensity maps of the two earthquakes were created.

The seismic intensity map for the  $M_w$  7.8 earthquake shows higher intensity in and around the NE-striking rupture fault(s) derived from the back-projection (Fig. 3), with the maximum intensity of IX. The intensity IX area is  $3260 \text{ km}^2$ , most of which are distributed in and to the southwest of the epicenter. The contour lines of the seismic intensity map for the  $M_w$  7.5 earthquake show elliptical shapes with the major axis trending W-E direction, in which the maximum intensity is IX. Due to the relatively small magnitude, the size of the area with intensity IX ( $379 \text{ km}^2$ ) is significantly smaller than those for the  $M_w$  7.8 earthquake.

We collected the population distribution in the grid area according to the Oak Ridge National Laboratory (ORNL, <https://landscan.ornl.gov>). Superimposing the population distribution on the seismic intensity map (Fig. 4), we got the number of exposed people in respective MMI values. We down-

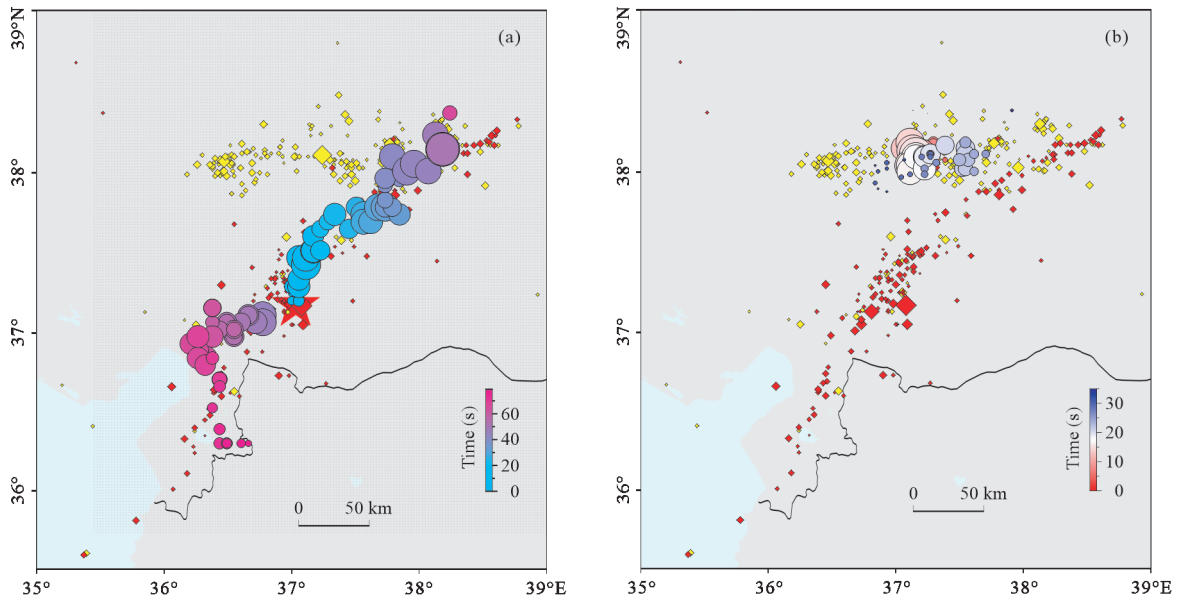


**Figure 2.** Time (color of the circles) and amplitudes (size of the circles) of the back-projection results for the  $M_w$  7.8 (a) and 7.5 (b) Turkey earthquakes. The seismic data recorded at Alaskan and Canadian stations were used in the back-projection. The red star indicates the epicenter determined by the USGS. The red, and yellow diamonds represent the aftershocks that occurred between the origin times of the  $M_w$  7.8 and 7.5 earthquakes, and in 15 h following the  $M_w$  7.5 earthquake (one day following the  $M_w$  7.8 earthquake) according to the EMSC.

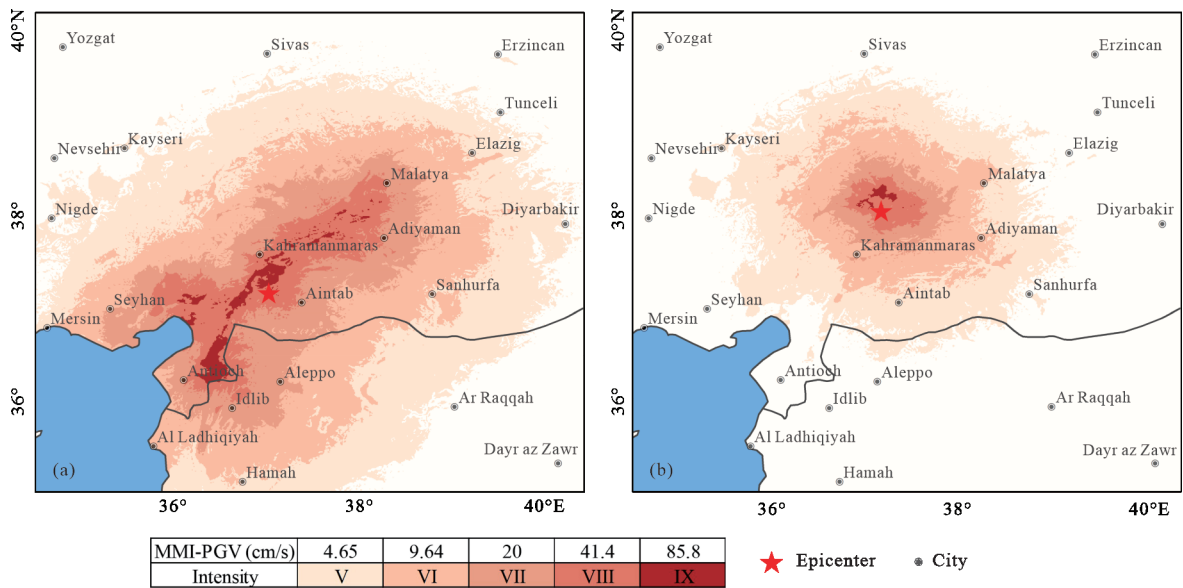


**Figure 3.**  $PGV_{v_{30}}$  estimates for the 2023  $M_w$  7.8 (a) and  $M_w$  7.5 (b) Turkey earthquakes. Red star indicates the earthquake epicenter. Black line represents the country border between Turkey and the Syrian Arab Republic.

loaded the PGAs and PGVs of the local strong motion observations from the USGS, to compare our calculated ground motions. The average residuals ( $\log_{10}(\text{obs./calc.})$ ) between our calculated and observed ground motions (PGA and PGV) in 300 km to epicenter were 0.043 and 0.319, respectively. The relatively small average residuals of the calculated ground motions validated our estimate of the ground motions (Fig. 5). The numbers of the exposed people in areas with intensity IX for the  $M_w$  7.8 and 7.5 earthquakes are 650 000, and 70 000, respectively. Those values are 2 570 000, and 140 000, in areas with intensity VIII, respectively. We then estimated the casualties of the two earthquakes using an empirical approach of Jaiswal et al.

(2009), the death toll from the two earthquakes is expected to exceed 21 000.

**DISCUSSION AND SUMMARY**

The 2023  $M_w$  7.8 (and 7.5) Turkey earthquake sequence is another large continental earthquake that caused catastrophic damages after the 2008  $M_w$  7.9 Wenchuan, China and the 2010  $M_w$  7.0 Haiti earthquake. Here we utilized the back-projection method and seismic data recorded in Alaskan and Canadian seismic stations, to resolve the ruptured faults of the two Turkey earthquakes.

The results showed that the  $M_w$  7.8 earthquake ruptured bi-

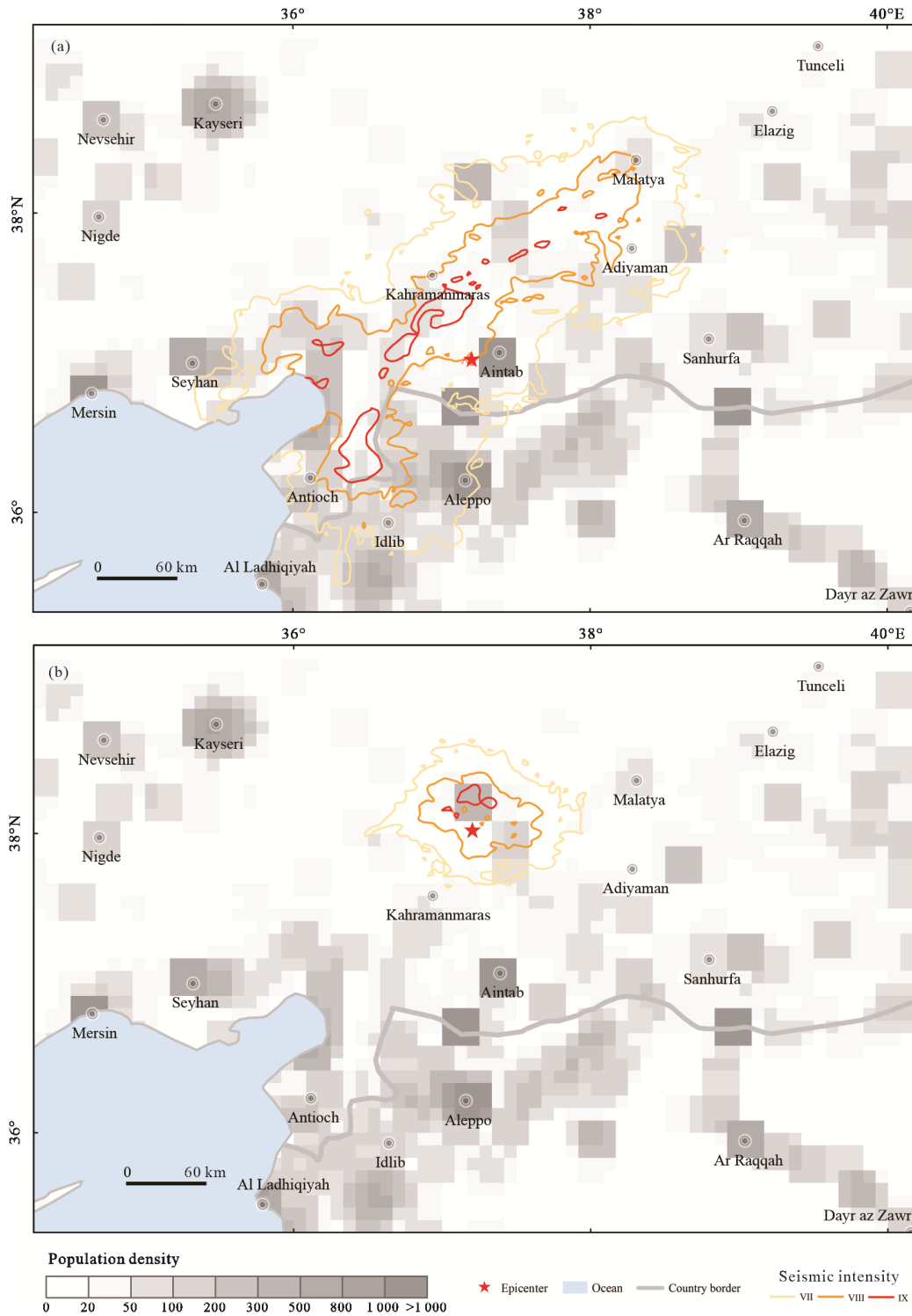


**Figure 4.** Exposed population in the  $M_w$  7.8 (a) and  $M_w$  7.5 (b) earthquakes. Colorful contour lines indicate the seismic intensity information of the  $M_w$  7.8 (a) and  $M_w$  7.5 (b) earthquakes. Population density is represented by the shade of gray.

laterally along the NE and SW directions, for about 140 and 130 km, respectively. The total rupture length and source duration were  $\sim 270$  km and 80 s, respectively. Based on the resolved fault patterns, we estimated the ground motions of the earthquakes and evaluated the casualties.

Without fault patterns, it is difficult to map the damaging zone accurately (Fig. 6a). That information could be incorporated in the ground motion estimations using source process deter-

mined by back-projection, stabilized finite slip inversion, locations of a few days' aftershocks, and/or field damage reports (Fig. 6b). The latest version of the ShakeMap that incorporated aftershock locations, field damage reports (DYFI), and other seismological observations show generally similar pattern of the seismic intensity map estimated from back-projection in this study (Fig. 6).

Among the approaches of estimating fault patterns, the

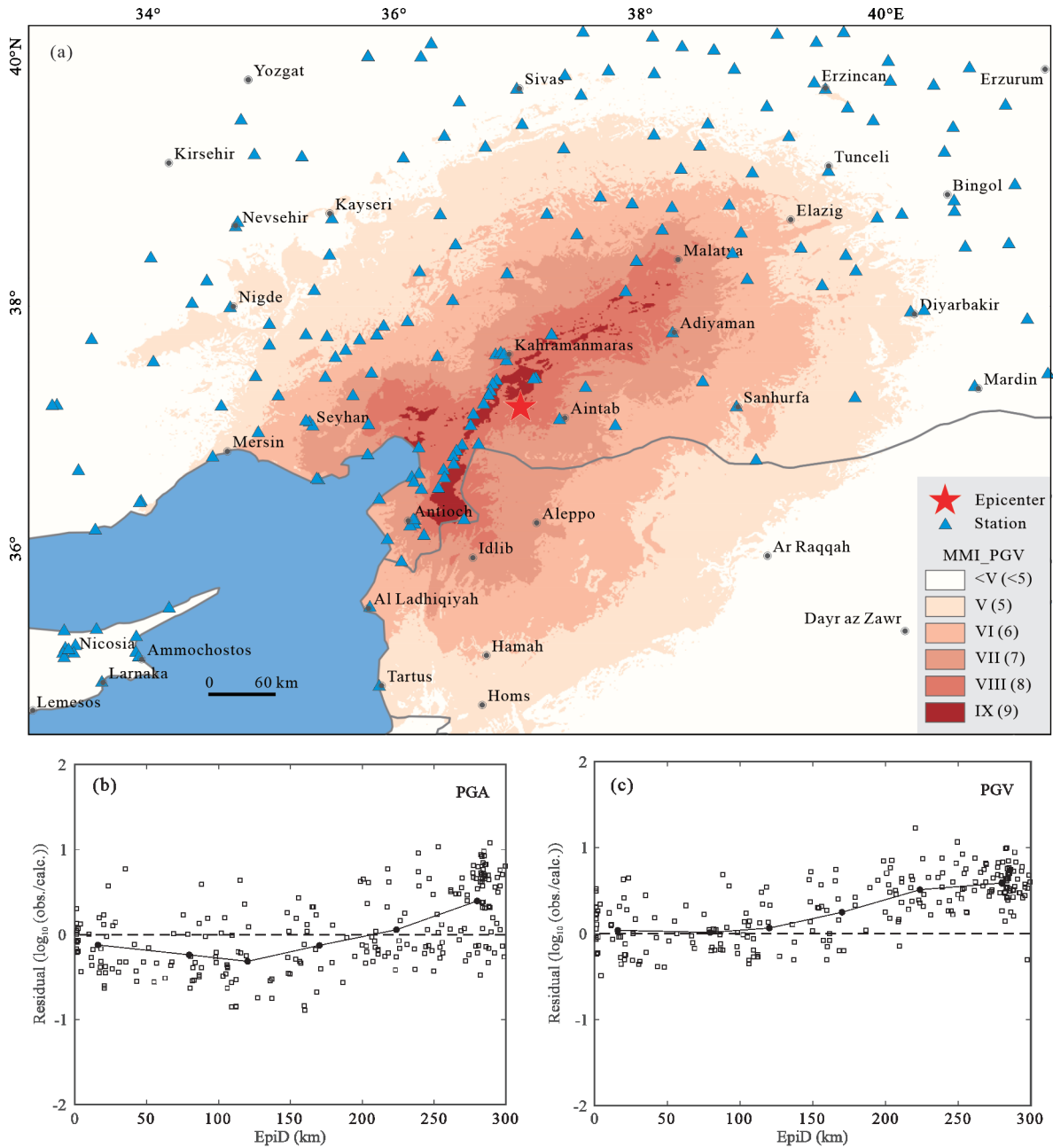


**Figure 5.** Comparison between instrument-recorded and calculated ground motions for the 2023  $M_w$  7.8 Turkey earthquake. (a) Blue triangle represents the strong-motion station and the background color represents the seismic intensities estimated in this study. The seismic observation data are collected from the USGS. The original data are from the Disaster and Emergency Management Authority (AFAD). (b) Residuals between the calculated and observed PGAs recorded during the  $M_w$  7.8 earthquake. Black dot and solid line are the mean residuals and their trendlines in (c) the same as in (b) except for PGVs.

back-projection offers promising results in quasi-real-time. Such efforts are valuable for immediate emergency response and rescue operation. For example, we determined the ground motion estimates of the  $M_w$  7.8 and 7.5 Turkey earthquakes in 2 h and 1 h following the earthquake origin times. The very fast ground motion map, together with the fault patterns, helped better estimate of the earthquake damages and rescue operations right after large earthquakes.

There are many factors influencing the assessment of earthquake casualties, which is technically very challenging. Earthquake intensity, seismic performance of buildings, population density, post-earthquake disasters, and site effects all affect

the results of casualty assessment. Here we rapidly assessed the casualty of the 2023  $M_w$  7.8 earthquake sequence as 21 000, which is in the same order of the number of casualty (~44 000, according to the Disaster and Emergency Management Authority (AFAD) up to Feb. 25, 2023) and is fairly good for emergency response right after the mainshock.

Another interesting phenomenon is the fault interaction among earthquake faults shown in the Turkey earthquake sequence. The  $M_w$  7.5 earthquake that was located ~95 km north to the epicenter, occurred ~9 h after the  $M_w$  7.8 earthquake. Likely the seismogenic fault for the  $M_w$  7.5 earthquake was triggered by the  $M_w$  7.8 earthquake. How the NE-striking faults

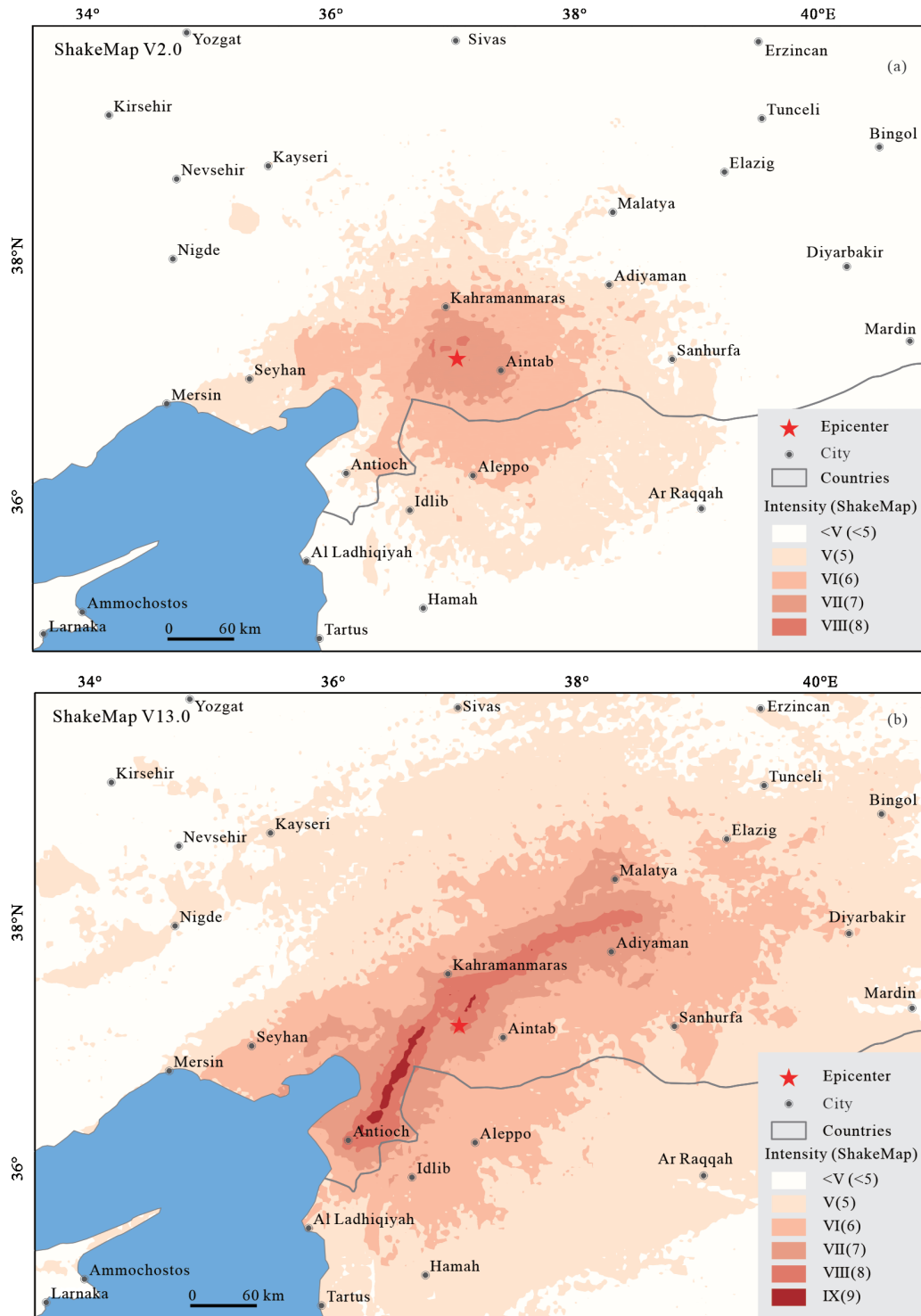


**Figure 6.** Evolution of the ShakeMap for the 2023  $M_w$  7.8 Turkey earthquake; (a) and (b) showing the two versions of the seismic intensity map (USGS, V2.0 and V13.0).

affects the EW-striking Cardak fault and nearby faults warrants further investigation.

**ACKNOWLEDGMENTS**

This study was supported by the Major Science and Technology Projects of Gansu Province (No. 21ZD4FA011), the National Natural Science Foundation of China (Nos. 41874062 and 41922025), and the National Key R & D Program of China

(No. 2017YFB0504104). We would like to thank Dr. Hongjun Si (Seismological Research Institute Inc., Japan) for related scientific discussion and suggestions. The final publication is available at Springer via <https://doi.org/10.1007/s12583-023-1316-6>.

**REFERENCES CITED**

Ambraseys, N. N., Jackson, J. A., 1998. Faulting Associated with Historical

- and Recent Earthquakes in the Eastern Mediterranean Region. *Geophysical Journal International*, 133(2): 390–406. <https://doi.org/10.1046/j.1365-246x.1998.00508.x>
- Busby, R. W., Aderhold, K., 2020. The Alaska Transportable Array: As Built. *Seismological Research Letters*, 91(6): 3017–3027. <https://doi.org/10.1785/0220200154>
- Chen, W. K., Wang, D., Si, H. J., et al., 2022a. Rapid Estimation of Seismic Intensities Using a New Algorithm that Incorporates Array Technologies and Ground-Motion Prediction Equations (GMPEs). *Bulletin of the Seismological Society of America*, 112(3): 1647–1661. <https://doi.org/10.1785/0120210207>
- Chen, W. K., Wang, D., Zhang, C., et al., 2022b. Estimating Seismic Intensity Maps of the 2021  $M_w$  7.3 Madoi, Qinghai and  $M_w$  6.1 Yangbi, Yunnan, China Earthquakes. *Journal of Earth Science*, 33(4): 839–846. <https://doi.org/10.1007/s12583-021-1586-9>
- Duman, T. Y., Emre, Ö., 2013. The East Anatolian Fault: Geometry, Segmentation and Jog Characteristics. *Geological Society, London, Special Publications*, 372(1): 495–529. <https://doi.org/10.1144/sp372.14>
- Fan, W. Y., Shearer, P. M., 2015. Detailed Rupture Imaging of the 25 April 2015 Nepal Earthquake Using Teleseismic P Waves. *Geophysical Research Letters*, 42(14): 5744–5752. <https://doi.org/10.1002/2015gl064587>
- Gülerce, Z., Tanvir Shah, S., Menekşe, A., et al., 2017. Probabilistic Seismic-Hazard Assessment for East Anatolian Fault Zone Using Planar Fault Source Models. *Bulletin of the Seismological Society of America*, 107(5): 2353–2366. <https://doi.org/10.1785/0120170009>
- Ishii, M., Shearer, P. M., Houston, H., et al., 2005. Extent, Duration and Speed of the 2004 Sumatra-Andaman Earthquake Imaged by the Hi-Net Array. *Nature*, 435(7044): 933–936. <https://doi.org/10.1038/nature03675>
- Jackson, J., McKenzie, D., 1984. Active Tectonics of the Alpine-Himalayan Belt between Western Turkey and Pakistan. *Geophysical Journal of the Royal Astronomical Society*, 77(1): 185–264. <https://doi.org/10.1111/j.1365-246x.1984.tb01931.x>
- Jaiswal, K., Wald, D. J., Hearne, M., 2009. Estimating Casualties for Large Earthquakes Worldwide Using an Empirical Approach. USGS Open—File Report 2009-1136. U.S. Geological Survey. <https://doi.org/10.3133/ofr20091136>
- Kang, D. J., Chen, W. K., Zhao, H. Q., et al., 2023. Rapid Assessment of the September 5, 2022  $M_s$  6.8 Luding Earthquake in Sichuan, China. *Earthquake Research Advances*, 100214. <https://doi.org/10.1016/j.eqrea.2023.100214>
- Kaymakci, N., Aldanmaz, E., Langereis, C., et al., 2007. Late Miocene Transcurrent Tectonics in NW Turkey: Evidence from Palaeomagnetism and  $^{40}\text{Ar}$ - $^{39}\text{Ar}$  Dating of Alkaline Volcanic Rocks. *Geological Magazine*, 144(2): 379–392. <https://doi.org/10.1017/s0016756806003074>
- Krüger, F., Ohrnberger, M., 2005. Tracking the Rupture of the  $M_w = 9.3$  Sumatra Earthquake over 1 150 km at Teleseismic Distance. *Nature*, 435(7044): 937–939. <https://doi.org/10.1038/nature03696>
- Lin, X., Hao, J. L., Wang, D., et al., 2021. Coseismic Slip Distribution of the 24 January 2020  $M_w$  6.7 Doganyol Earthquake and in Relation to the Foreshock and Aftershock Activities. *Seismological Research Letters*, 92(1): 127–139. <https://doi.org/10.1785/0220200152>
- McKenzie, D. P., 1972. Active Tectonics of the Mediterranean Region. *Geophysical Journal of the Royal Astronomical Society*, 30(2): 109–185. <https://doi.org/10.1111/j.1365-246x.1972.tb02351.x>
- McKenzie, D. P., 1976. The East Anatolian Fault: a Major Structure in Eastern Turkey. *Earth and Planetary Science Letters*, 29(1): 189–193. [https://doi.org/10.1016/0012-821x\(76\)90038-8](https://doi.org/10.1016/0012-821x(76)90038-8)
- Meng, L. S., Zhang, A. L., Yagi, Y., 2016. Improving back Projection Imaging with a Novel Physics-Based Aftershock Calibration Approach: A Case Study of the 2015 Gorkha Earthquake. *Geophysical Research Letters*, 43(2): 628–636. <https://doi.org/10.1002/2015gl067034>
- Midorikawa, S., 1994. Site Effects on Strong-Motion Records Observed during the 1987 Chiba-Ken-Toho-Oki, Japan Earthquake. *Environmental Science*, 9(3): 85–90
- Milkereit, C., Grosser, H., Wang, R. J., et al., 2004. Implications of the 2003 Bingol Earthquake for the Interaction between the North and East Anatolian Faults. *Bulletin of the Seismological Society of America*, 94(6): 2400–2406. <https://doi.org/10.1785/0120030194>
- Okuwaki, R., Kasahara, A., Yagi, Y., et al., 2019. Backprojection to Image Slip. *Geophysical Journal International*, 216(3): 1529–1537. <https://doi.org/10.1093/gji/ggy505>
- Reilinger, R., McClusky, S., Vernant, P., et al., 2006. GPS Constraints on Continental Deformation in the Africa-Arabia-Eurasia Continental Collision Zone and Implications for the Dynamics of Plate Interactions. *Journal of Geophysical Research: Solid Earth*, 111(B5): B05411. <https://doi.org/10.1029/2005jb004051>
- Satriano, C., Kiraly, E., Bernard, P., et al., 2012. The 2012  $M_w$  8.6 Sumatra Earthquake: Evidence of Westward Sequential Seismic Ruptures Associated to the Reactivation of a N-S Ocean Fabric. *Geophysical Research Letters*, 39(15): L15302. <https://doi.org/10.1029/2012gl052387>
- Si, H., Midorikawa, S., 1999. New Attenuation Relationships for Peak Ground Acceleration and Velocity Considering Effects of Fault Type and Site Condition. *Journal of Structural and Construction Engineering (Transactions of Aij)*, 64: 63–70. [https://doi.org/10.3130/AIJS.64.63\\_2](https://doi.org/10.3130/AIJS.64.63_2)
- Vallée, M., Landès, M., Shapiro, N. M., et al., 2008. The 14 November 2001 Kokoxili (Tibet) Earthquake: High-Frequency Seismic Radiation Originating from the Transitions between Sub-Rayleigh and Supershear Rupture Velocity Regimes. *Journal of Geophysical Research: Solid Earth*, 113(B7): B07305. <https://doi.org/10.1029/2007jb005520>
- Wang, D., Kawakatsu, H., Zhuang, J. C., et al., 2017. Automated Determination of Magnitude and Source Length of Large Earthquakes Using Backprojection and P Wave Amplitudes. *Geophysical Research Letters*, 44(11): 5447–5456. <https://doi.org/10.1002/2017gl073801>
- Wang, D., Mori, J., 2016. Short-Period Energy of the 25 April 2015  $M_w$  7.8 Nepal Earthquake Determined from Backprojection Using Four Arrays in Europe, China, Japan, and Australia. *Bulletin of the Seismological Society of America*, 106(1): 259–266. <https://doi.org/10.1785/0120150236>
- Worden, C. B., Gerstenberger, M. C., Rhoades, D. A., et al., 2012. Probabilistic Relationships between Ground-Motion Parameters and Modified Mercalli Intensity in California. *Bulletin of the Seismological Society of America*, 102(1): 204–221. <https://doi.org/10.1785/0120110156>
- Xu, J., Liu, C. L., Xiong, X., 2020. Source Process of the 24 January 2020  $M_w$  6.7 East Anatolian Fault Zone, Turkey, Earthquake. *Seismological Research Letters*, 91(6): 3120–3128. <https://doi.org/10.1785/0220200124>
- Yao, H. J., Gerstoft, P., Shearer, P. M., et al., 2011. Compressive Sensing of the Tohoku-Oki  $M_w$  9.0 Earthquake: Frequency-Dependent Rupture Modes. *Geophysical Research Letters*, 38(20): L20310. <https://doi.org/10.1029/2011gl049223>
- Zhang, H., Ge, Z., 2010. Tracking the Rupture of the 2008 Wenchuan Earthquake by Using the Relative Back-Projection Method. *Bulletin of the Seismological Society of America*, 100(5B): 2551–2560. <https://doi.org/10.1785/0120090243>